IVYSPRING INTERNATIONAL PUBLISHER

Theranostics

2018; 8(3): 663-675. doi: 10.7150/thno.21927

Research Paper

Mesoporous Carbon Nanospheres as a Multifunctional Carrier for Cancer Theranostics

Libo Zhou[1], Ying Jing[1], Yubin Liu[3], Zhihe Liu[1], Duyang Gao[3], Haobin Chen[1], Weiye Song[1], Tao Wang[1], Xiaofeng Fang[1], Weiping Qin[1], Zhen Yuan[3], Sheng Dai[4], Zhen-An Qiao[1]✉ and Changfeng Wu[2]✉

1. State Key Laboratory on Integrated Optoelectronics, College of Electronic Science and Engineering; State Key Laboratory of Inorganic Synthesis and Preparation Chemistry, College of Chemistry, Jilin University, Changchun 130012, China;
2. Department of Biomedical Engineering, Southern University of Science and Technology, Shenzhen 518055, China;
3. Bioimaging Core, Faculty of Health Science, University of Macau Taipa, Macau SAR, 999078, China;
4. Chemical Sciences Division, Oak Ridge National Laboratory, Oak Ridge, TN, 37831, USA.

✉ Corresponding authors: Zhen-An Qiao, E-mail: qiaozhenan@jlu.edu.cn Changfeng Wu, E-mail: wucf@sustc.edu.cn

Received: 2017.07.15; Accepted: 2017.10.27; Published: 2018.01.01

Abstract

Optical nanomaterials with intense absorption in near-infrared (NIR) region hold great promise for biomedical applications such as photothermal therapy (PTT) and photoacoustic imaging (PAI). In this work, we report mesoporous carbon nanospheres (Meso-CNs) with broadband and intense absorption in the UV–Vis–NIR region (300–1400 nm) and explore their potential as a multifunctional platform for photoacoustic imaging and chemo-photothermal therapy.

Methods: Meso-CNs were prepared by a "silica-assisted" synthesis strategy and characterized by transmission electron microscope and optical spectroscopy. We investigated the photothermal conversion and photoacoustic imaging of Meso-CNs in comparison with single-walled carbon nanotubes (SWCNTs), graphene and gold nanorods (GNRs). In vitro cellular assays and in vivo chemo-photothermal combination therapy were performed.

Results: The absorption coefficients of Meso-CNs are 1.5–2 times higher than those of SWCNTs and graphene and are comparable to those of GNRs in both the first and the second near-infrared optical windows (NIR-I and NIR-II) of tissues. When exposed to an NIR laser, the photothermal and photoacoustic signal generation of Meso-CNs are also stronger than those of SWCNTs, graphene, and GNRs. DOX was loaded into Meso-CNs with a high efficiency (35 wt%) owing to the unique mesoporous structure. Particularly, the drug release from Meso-CNs is sensitive to both pH and NIR light stimulation. In vivo chemo-photothermal combination therapy demonstrates a remarkable inhibition effect on tumor growth under NIR laser treatment.

Conclusions: We have developed Meso-CNs for photothermal conversion and photoacoustic imaging. The porous structure also serves as a drug carrier and the drug release can be controlled by pH and external light. The high drug loading capacity, superior photothermal and photoacoustic generation, together with the apparent chemo-photothermal therapeutic effect, make Meso-CNs a promising platform for cancer theranostics.

Key words: mesoporous carbon nanospheres, near-infrared absorption, drug delivery, photoacoustic imaging, photothermal therapy.

Introduction

Optical materials with strong absorption have attracted a considerable amount of attention because of their widespread applications such as photocatalysis [1-3], solar cells [4-6], and photonic devices [7, 8]. Particularly, nanomaterials with intense absorption in the near-infrared (NIR) region are promising for biomedical applications including photothermal therapy (PTT) and photoacoustic imaging (PAI) [9-12]. PTT is a newly developed treatment modality that is minimally invasive compared to other cancer therapies such as radiotherapy and surgery. The nanomaterials used in PTT can generate heat under light irradiation to increase the local temperature of a tumor and kill

cancer cells [13-17]. PAI has emerged as a novel imaging modality that integrates optical excitation with ultrasonic detection, which provides deep tissue penetration and a high spatial resolution for theranostics [18-23]. Because a photoacoustic signal is primarily determined by the thermal expansion induced by a pulsed laser, the contrast agents for PAI are naturally applicable to PTT, which endows photothermal materials with a key position in optical theranostic systems [24, 25].

Currently, there is a large amount of interest in the development of various light-absorbing materials such as metallic nanoparticles [26-31], semiconducting polymer nanoparticles [32-36], and carbon-based nanostructures [37-39]. Notably, carbon-based nanostructures have received tremendous attention owing to their outstanding physical and chemical properties. Carbon nanotubes (CNTs) and graphene have been widely used in biomedical imaging and phototherapy applications. In 2005, DNA-coated single-walled carbon nanotubes (SWCNTs) were first developed by Dai and coworkers for *in vitro* cancer cell PTT [40]. Since then, many different groups have explored PTT using various bioconjugated CNTs as photothermal agents [41-45]. Encouraged by the successful use of CNTs for biomedical applications, graphene has also provided many new opportunities in biomedicine. Since 2008, a large number of groups have reported graphene- and graphene oxide (GO)-based biomedical applications including biosensing [46, 47], bioimaging [48, 49], drug and gene delivery [50-53], and PTT cancer treatment [54-58]. Despite the widespread investigations of CNTs and graphene in biomedical research, their practical applications are constrained by their poor dispersity and stability in aqueous solutions.

Here, we report colloidal mesoporous carbon nanospheres (Meso-CNs) in the form of stable suspensions exhibiting broadband and intense absorption in the UV–Vis–NIR region. We performed side-by-side comparisons of photothermal conversion and photoacoustic generation from the Meso-CNs with SWCNTs, graphene, and gold nanorods (GNRs). The Meso-CNs possess absorption coefficients that are 1.5–2 times higher than those of CNTs and graphene in the broad wavelength region and are comparable to those of GNRs in both the first and second NIR optical windows (NIR-I and NIR-II) of biological tissue. The anticancer drug doxorubicin (DOX) was loaded into Meso-CNs with a high efficiency (35 wt%) owing to the large surface area, appropriate pore sizes and large pore volume of Meso-CNs. A combination therapy was finally carried out with DOX-loaded Meso-CNs, demonstrating an apparent tumor-suppression effect by using a relatively low drug dosage and laser power density. The high drug loading capacity, together with the excellent photothermal and photoacoustic signal generation, makes Meso-CNs a promising platform for cancer theranostic applications.

Results and Discussion

Synthesis and characterizations of Meso-CNs

Meso-CNs were prepared by an effective approach called the "silica-assisted" synthesis strategy (Figure 1A) [59]. Both transmission electron microscopy (TEM) and scanning electron microscopy (SEM) were used to characterize the morphology of the Meso-CNs. The obtained Meso-CNs are monodisperse and have a uniform particle size of 200 nm with a well-defined spherical morphology (Figure 1B, Figure S1A). A large number of mesopores can be clearly observed from the spherical framework, and the pore size is roughly estimated to be ~2.5 nm (Figure S1B, C). For comparison, microporous carbon nanospheres (Micro-CNs) with a similar size of 200 nm were prepared in the absence of silica and a surfactant (Figure 1C). The N_2 adsorption−desorption isotherm of the Meso-CNs (Figure 1D) exhibits a typical type-IV hysteresis, indicative of the presence of mesopores. It can be seen that the adsorption isotherm shows an apparent capillary condensation step at a relative pressure (P/P_0) of 0.14−0.32, corresponding to a pore size of 2.5 nm, as calculated with the Barrett−Joyner−Halenda (BJH) method. The isotherm of the Micro-CNs shows a type-I reversible sorption profile, indicating a microporous structure. The Brunauer–Emmett–Teller (BET) surface areas of the Meso-CNs and Micro-CNs are 1044 m^2/g and 435 m^2/g, and the total pore volumes are approximately 0.6174 cm^3/g and 0.2613 cm^3/g.

The X-ray diffraction (XRD) patterns reveal that both the Meso-CNs and Micro-CNs possess an amorphous nature (Figure 1E). In addition, no obvious peak was observed in the small-angle X-ray scattering (SAXS) spectrum of the Meso-CNs (Figure S1D), indicating the mesopores in Meso-CNs are not ordered. Raman spectroscopy of the Meso-CNs and Micro-CNs show typical D and G bands at 1350 cm^{-1} and 1580 cm^{-1} (Figure S1E), which are consistent with other carbon materials. The C1s X-ray photoelectron spectroscopy (XPS) data for the Meso-CNs reveal that the carbon surface is dominated with C−C or C−H species (284.8 eV) along with smaller concentrations of C−O (286.2 eV) and O−C=O (288.5 eV) originating from the reaction of HF with carbon during the removal of silica (Figure 1F). Therefore, compared to Micro-CNs or other carbon nanomaterials such as SWCNTs and graphene, Meso-CNs exhibit excellent

dispersibility in water because of their highly negative surface zeta potential of -35.5 mV (Figure S2A). The colloidal solutions of Meso-CNs are stable for more than one month without sign of agglomeration (Figure S2B). Optical density of Meso-CNs and Micro-CNs was measured when they were dispersed in water at the same concentration (30 μg/mL). The results showed that the optical density of Meso-CNs was approximately five times higher than that of Micro-CNs (Figure 1G). Therefore, the high absorption of Meso-CNs is likely related to their unique mesoporous structure and high surface area, although the exact mechanism needs to be further investigated.

Optical properties and photothermal conversion of Meso-CNs

We investigated the optical absorption and photothermal conversion of Meso-CNs. Other carbon materials (SWCNTs and graphene), GNRs with an absorption peak at 808 nm (GNR808), and GNRs with an absorption peak at 1120 nm (GNR1120) were used for comparison. It is notable that the Meso-CNs are well-dispersed in water without the use of a surfactant, indicating their hydrophilic surfaces. In contrast, SWCNTs and graphene are typically hydrophobic and significant surface modifications (or surfactants) are required to disperse them in an aqueous solution. UV–Vis–NIR absorption spectra show that the Meso-CNs possess a broad absorption band from the UV to NIR wavelength range (300–1400 nm) (Figure 2A, B). Carbon spheres, porous carbon spheres, and nanosized carbon dots have been extensively explored by many groups [60-64]. Typically, these carbon materials exhibit strong UV absorption and negligible absorption in the NIR region. The broadband absorption of Meso-CNs is distinct from previously reported carbon spheres and nanodots in that they possess intense absorption in both the NIR-I and NIR-II optical windows. Their broad and intense NIR absorption makes Meso-CNs a highly promising PTT agent for cancer therapy. The absorption coefficients of the Meso-CNs were determined to be 33.9 L $g^{-1}cm^{-1}$ and 29.1 L $g^{-1}cm^{-1}$ at 808 nm and 1120 nm, respectively. The absorption coefficients of the Meso-CNs and other agents are presented in Figure S3 and Table S1, which clearly indicates that the absorption coefficients of the Meso-CNs are 1.5–2 times higher than those of SWCNTs and graphene and are comparable to the peak absorption coefficients of GNR808 and GNR1120. The superior optical absorption of the Meso-CNs are promising for PTT and PAI applications in both the NIR-I and NIR-II optical windows.

To evaluate their photothermal conversion, a Meso-CN solution was exposed to laser irradiation at 808 nm (1.0 W/cm^2, 10 min) and 1120 nm (0.5 W/cm^2, 10 min), respectively. A power density of 1.0 W/cm^2 is usually used for 808 nm NIR laser-induced heat conversion [10, 65]. As shown in Figure 2C, the temperature of the aqueous Meso-CN dispersion increased by 48 °C after 808 nm laser irradiation. In contrast, the temperature of pure water increased by only 9 °C. For 1120 nm laser irradiation, the temperature of the aqueous Meso-CN dispersion also increased more rapidly than suspensions of other materials (Figure 2D). Thus, the Meso-CNs are able to convert NIR laser energy into heat efficiently owing to their strong absorption in the NIR region. The Meso-CNs solution was also exposed to an 808 nm laser irradation at a power density of 0.5 W/cm^2 for 10 min. As shown in Figure S4A, the sample solution upon 808 nm laser irradiation shows a higher rate regarding the temperature rise than that by 1120 nm at the same power density. This is mainly due to the larger absorption coefficient of Meso-CNs at 808 nm as compare to that at 1120 nm. For pure water sample, 1120 nm laser have a higher photothermal conversion rate than 808 nm, which may be a disadvantage. However, the laser irradiation in the NIR-II region has a deep penetration owing to the reduced scattering and absorption of biological tissue. Therefore, we chose both of the two lasers for the following experiments. The excellent photothermal conversion ability of Meso-CNs were further confirmed by IR thermal imaging and photothermal conversion curves of the Meso-CNs aqueous dispersions. The IR thermal images and photothermal conversion curves of Meso-CNs show an obvious concentration-dependent heating effect of Meso-CNs (Figure 2E, F, Figure S4B, C). Photothermal response curves of the Meso-CNs by turning the laser irradiation on and off are shown in Figure S4D, E. According to a previously reported method [65, 66], the photothermal conversion efficiency (η) values of the Meso-CNs at 808 nm and 1120 nm were calculated to be 35.8% and 46.3%, respectively. These values are comparable to or slightly higher than those of graphene, SWCNTs and GNRs under the same experimental conditions. We examined the photostability of the Meso-CNs, which were irradiated with 808 nm and 1120 nm lasers for 30 min, respectively. The UV-Vis-NIR absorption and the particle size distribution of Meso-CNs were measured before and after laser irradiation (Figure S5). No significant difference was observed before and after laser irradiation, indicating the good photostability of Meso-CNs. The large absorption coefficients and high photothermal conversion efficiencies of the Meso-CNs indicate their great potential for PTT and PAI applications.

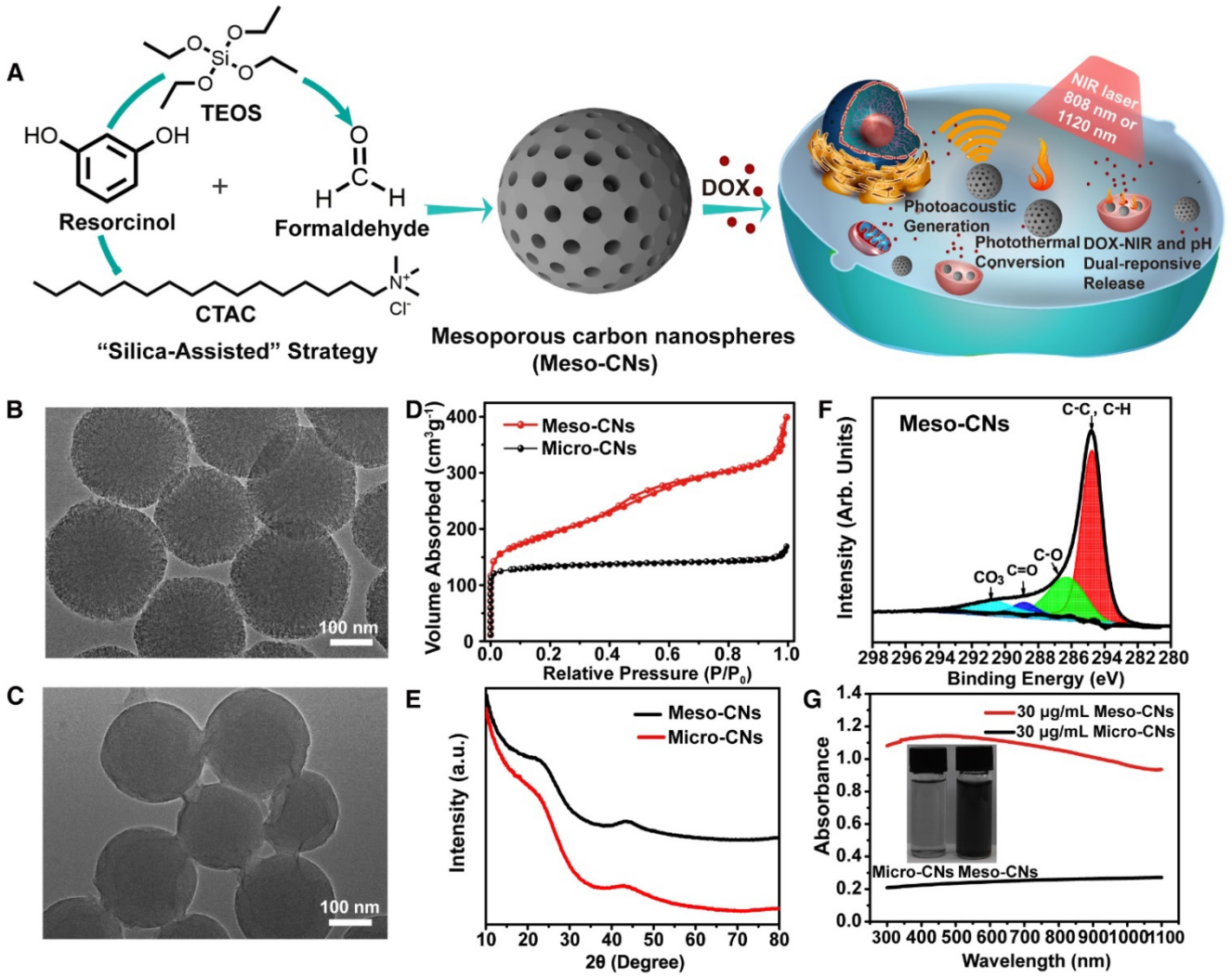

Figure 1. Synthesis and characterization of Meso-CNs and Micro-CNs. (A). Synthesis and application scheme for Meso-CNs as photoacoustic agents and chemo-photothermal cancer therapy platforms. **(B).** Typical TEM image of the Meso-CNs. **(C).** Typical TEM image of Micro-CNs. **(D)** N_2 adsorption−desorption isotherms of the Meso-CNs and Micro-CNs. **(E)**. XRD patterns of the Meso-CNs and Micro-CNs. **(F).** XPS spectra of the Meso-CNs. **(G).** Absorption spectra of the Meso-CNs and Micro-CNs dispersed in water at a concentration of 30 μg/mL. The inset shows a photograph of Meso-CN and Micro-CN aqueous solutions at a concentration of 30 μg/mL.

In vitro photothermal therapy of Meso-CNs

The cytotoxicity of the Meso-CNs in MCF7 and HeLa cancer cells was evaluated using standard 3-(4,5-dimethylthiazol-2-yl)-2,5-diphenyltetrazolium bromide (MTT) assays. The Meso-CNs did not show cytotoxicity when the cells were incubated with a high concentration of 200 μg/mL for 24 h. The viabilities of the MCF7 and Hela cells were both >90%, suggesting good biocompatibility with the Meso-CNs (Figure 3A). The *in vitro* photothermal effect of the Meso-CNs was then examined by the MTT assay again. The results demonstrate that the MCF7 and Hela cells were killed in a concentration-dependent manner after NIR light-induced PTT with Meso-CNs. Both types of cells showed remarkably reduced viabilities when the Meso-CN concentration was as low as 30 μg/mL (Figure 3B). Moreover, cell staining was performed to confirm the photothermal effect of the Meso-CNs. The live/dead cells were differentiated by calcein-AM (live cells, green fluorescence) and propidium iodide (PI; dead cells, red fluorescence) co-staining using fluorescence confocal microscopy. The staining results indicated a dose-dependent PTT effect after the cells were exposed to both 808 nm and 1120 nm light irradiation. Almost all of the cells were killed after incubation with a Meso-CN concentration of 30 μg/mL followed by PTT treatment (Figure 3C, D). These results indicate that Meso-CNs exhibited excellent photothermal effects that can be conveniently adjusted by both NIR-I and NIR-II light irradiation.

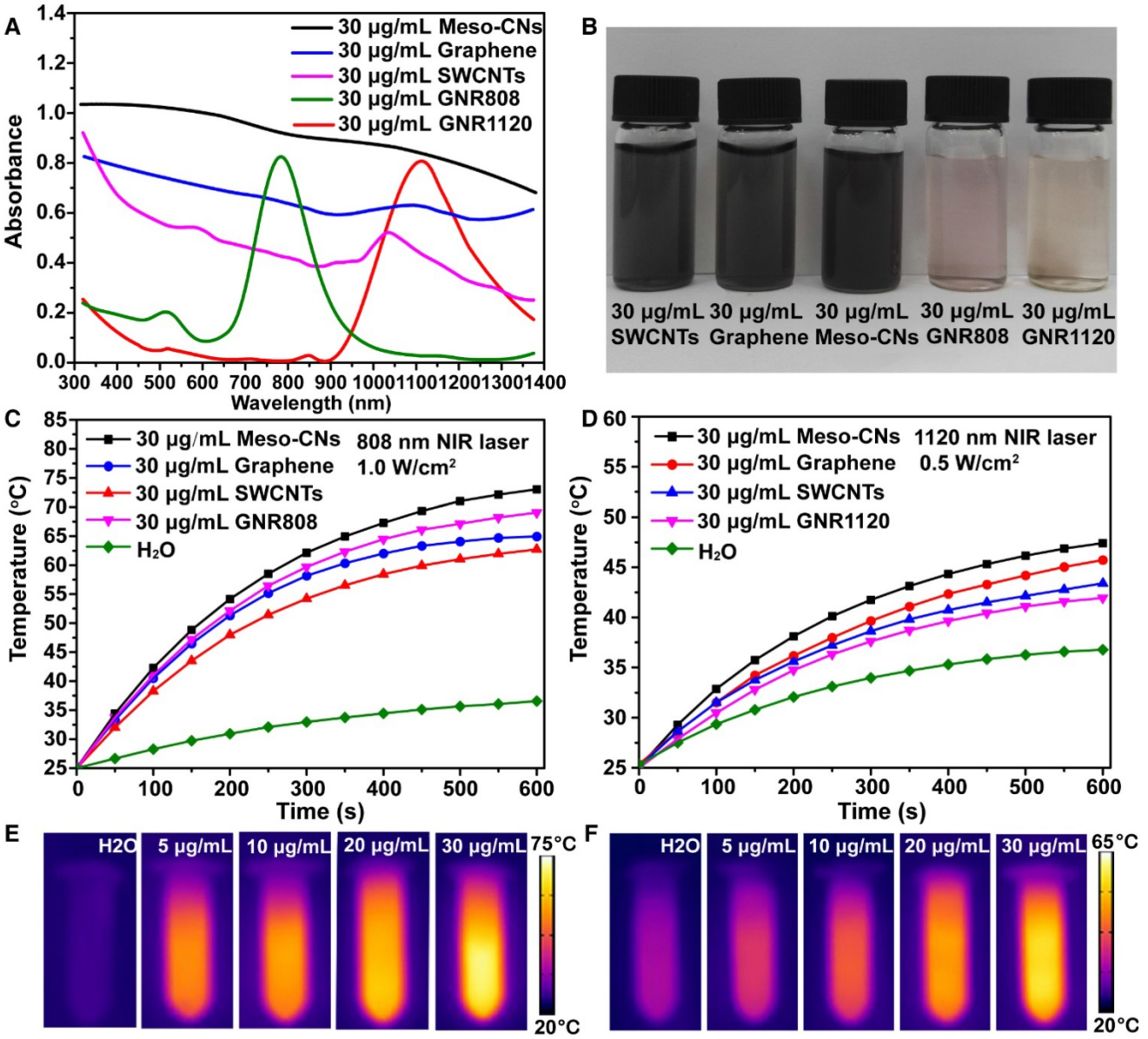

Figure 2. NIR optical properties and photothermal characterization. (A) UV–Vis–NIR absorption spectra of Meso-CNs and other photothermal contrast agents (graphene, SWCNTs, GNR808, and GNR1120) dispersed in water at 30 μg/mL. **(B)**. Photograph of Meso-CNs and other contrast photothermal agents dispersed in water at 30 μg/mL. Photothermal conversion curves of Meso-CNs and other contrast photothermal agents under irradiation with **(C)** 808 nm (1.0 W/cm²) and **(D)** 1120 nm (0.5 W/cm²) lasers. IR thermal images of pure water and Meso-CN solutions at different concentrations (5, 10, 20, and 30 μg/mL) under **(E)** 808 nm laser irradiation at a power density of 1.0 W/cm² and **(F)** 1120 nm laser irradiation at a power density of 0.5 W/cm² for 3 min.

Light and pH controlled drug release

Because of their unique mesoporous structure, we investigated the drug loading and release behaviors using Meso-CNs as a drug carrier. Meso-CNs were mixed with the anticancer drug DOX and stirred for 24 h at room temperature. Free DOX molecules were removed by centrifugation and the drug loading capacity was calculated by the UV-Vis absorption spectra (Figure S6). The DOX-loaded Meso-CNs exhibited a characteristic absorption peak for DOX at 480 nm, indicating successful drug loading (Figure 4A). As shown in Table S2, the loading capacity of DOX in Meso-CNs was calculated to be ~35.0 wt% (35 mg DOX per 100 mg Meso-CNs), which is higher than that of the previously reported mesoporous carbon–silica nanocapsules (~23.0%) [67]. The DOX release behavior was further examined for the Meso-CNs in acidic (pH: 5.2) and neutral solutions (pH: 7.3) with NIR light irradiation. Figure 4B shows that the release of DOX is very slow in the neutral condition. However, enhanced DOX release was observed when the pH of the dispersion media (PBS) was adjusted to be mildly acidic. The amounts of DOX released after 24 h were 14% for a pH of 7.3 and 26% for a pH of 5.2. The pH-dependent drug release behavior of DOX can be attributed to the weakened

hydrogen bonds and electrostatic interactions between DOX and Meso-CNs with decreasing pH [9, 52]. To examine the light-controlled drug release, DOX-loaded Meso-CNs were dispersed in a PBS buffer (pH: 5.2, 37 °C) and then exposed to the 808 nm and 1120 nm lasers (0.5 W/cm²) at different time intervals. Out results indicate that the release of DOX from the Meso-CNs can be repeatedly triggered by both lasers. The amounts released by the two laser treatment groups were ~32%, which is 1.2 times higher than for the same conditions without laser irradiation (26%) and 2.3 times higher than that of the group at a neutral pH of 7.3 without laser irradiation (14%) (Table S3). The photo-induced enhancement of DOX release is likely due to the thermal expansion of the porous structure of Meso-CNs. The temperature increase can also reduce the interactions between DOX and Meso-CNs owing to increased vibrations of DOX and Meso-CNs. Owing to the slightly acidic pH in the tumor microenvironment and the endosomes/lysosomes inside cells, the pH-dependent DOX release behavior from the Meso-CNs provides the ability for controlled drug release inside tumor tissue by NIR lasers. The intracellular drug release of DOX from the Meso-CNs in cellular assays was evaluated. MCF7 cells were incubated with DOX-loaded Meso-CNs for 5 h, washed with PBS, and then stained with nucleus dye H33258. Confocal fluorescence imaging showed that DOX molecules were efficiently released from the Meso-CNs and entered the nuclei, indicating successful DOX delivery. The high loading capacity and the pH/light double-controlled release make Meso-CNs a unique platform for drug delivery (Figure 4C, D).

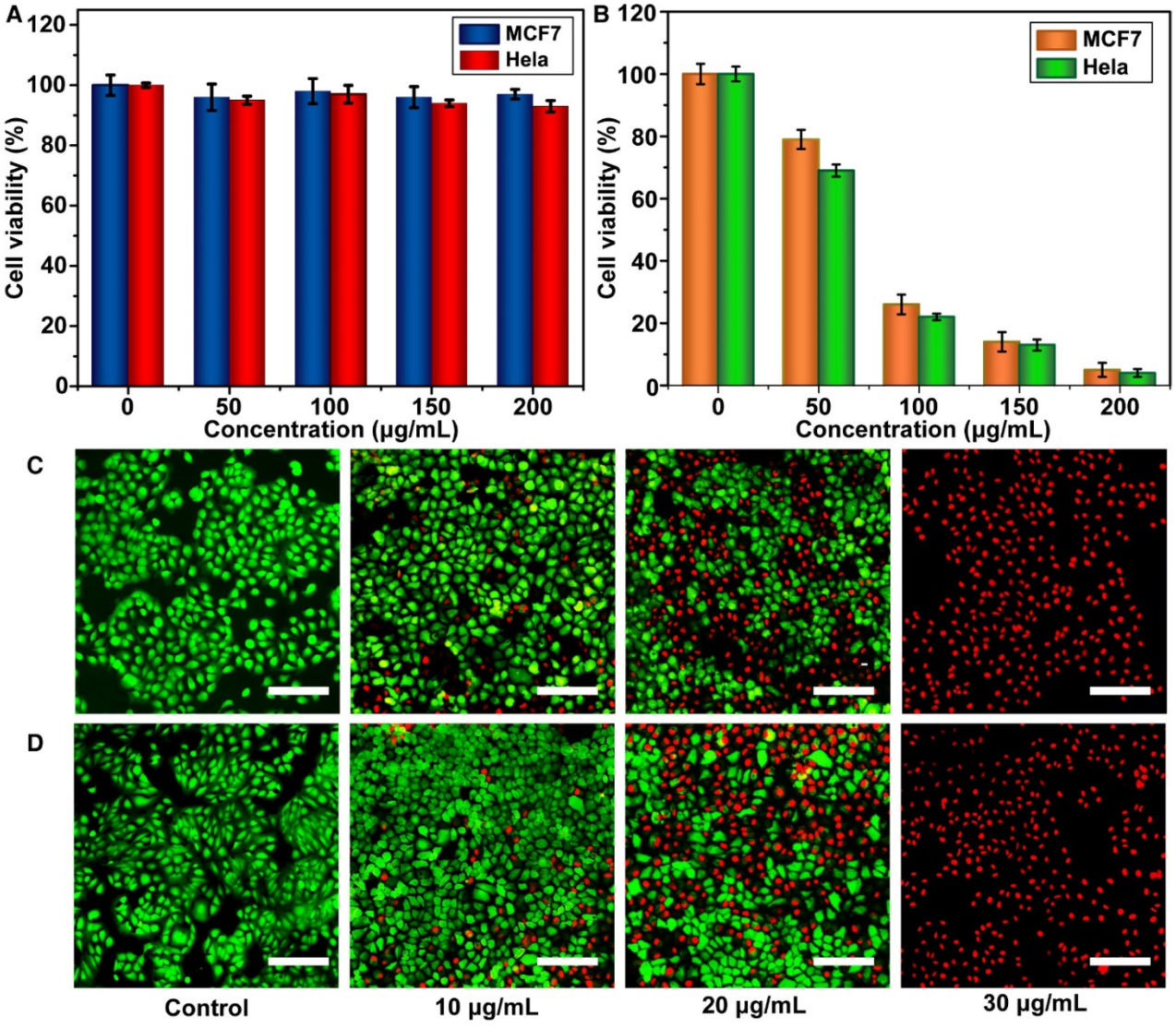

Figure 3. ***In vitro*** **cytotoxicity and photothermal therapy effect. (A)** Relative viabilities of MCF7 and Hela cells after incubation with various concentrations of Meso-CNs for 24 h. **(B)**. Relative viabilities of MCF7 and Hela cells after incubation with different concentrations of Meso-CNs and subsequent exposure to 650 nm light at a power density of 0.3 W/cm² for 30 min. Confocal images of Calcein AM/PI-stained MCF7 cancer cells after incubation with different concentrations of Meso-CNs and irradiation with **(C)** a 808 nm laser at 1.0 W/cm² for 10 min and **(D)** a 1120 nm laser at 0.5 W/cm² for 20 min. Scale bar: 150 μm.

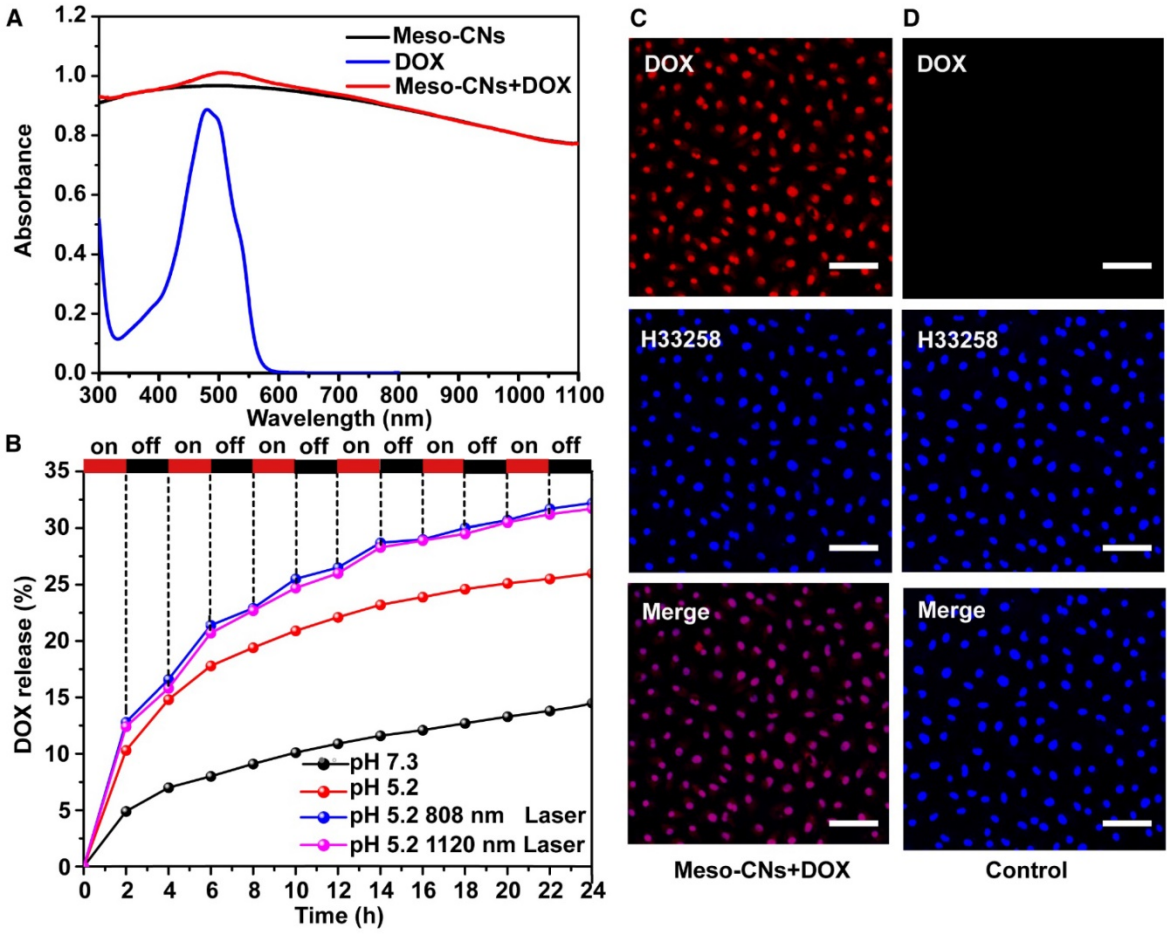

Figure 4. Meso-CN-based drug loading and multiple stimuli-responsive drug release. (A) UV–Vis–NIR absorption spectra of Meso-CNs, DOX and DOX loaded Meso-CNs. **(B)**. Cumulative release profiles of DOX-loaded Meso-CNs in different pH and laser irradiation conditions. Both the 808 nm and 1120 nm lasers with a power density of 0.5 W/cm² were used for light-dependent drug release experiments. **(C)**. Confocal images of MCF7 cells incubated with DOX-loaded Meso-CNs for 5 h. **(D)**. Confocal images of MCF7 cells incubated with Meso-CNs for 5 h. The red and blue colors indicate DOX fluorescence and H33258-stained nuclear fluorescence, respectively. Scale bar: 50 μm.

Photoacoustic imaging of Meso-CNs

Next, we explored the photoacoustic generation of Meso-CNs in both a phantom and living mice. The photoacoustic properties of the Meso-CNs and other contrast agents (graphene, SWCNTs and GNR808) were investigated under 808 nm laser excitation. At the same mass concentrations (25 μg/mL) in agar phantoms, the photoacoustic amplitude of the Meso-CNs was ~1.2, ~1.6, and ~2.1 times higher than those of graphene, SWCNTs, and GNR808, respectively (Figure 5A, B). The photoacoustic generation was further examined after subcutaneous injections of Matrigel-containing solutions of Meso-CNs, graphene, SWCNTs, or GNR808 at the same concentration (50 μg/mL) (Figure 5C). The mouse injected with Meso-CNs showed much higher photoacoustic signals than those injected with the other materials, which is consistent with the results from the phantom experiment (Figure 5D). Therefore, the efficient photoacoustic generation by the Meso-CNs represents a significant advance in high-sensitivity PAI, with potential clinical diagnostic applications.

In vivo photothermal therapy

Finally, we performed *in vivo* PTT with H22 tumor-bearing ICR mice. An H22 tumor model was developed by subcutaneous injection with H22 hepatoma ascites (120 μL/mouse) into the backside of each ICR mouse. When the tumor volume reached 120 mm³, the mice were divided into seven groups and intratumorally injected with PBS, Meso-CNs, or DOX-loaded Meso-CNs. Several groups of mice were irradiated with the 808 nm or 1120 nm laser at a power density of 0.5 W/cm² for 20 min. As shown in Figure 6A, the local temperature of the tumors injected with Meso-CNs and DOX-loaded Meso-CNs rapidly rose to 65 °C, whereas the tumors injected with PBS showed only a little increase under the same irradiation conditions. After receiving various treatments, the tumor sizes and body weights of the

mice were measured every 2 days. There were no statistically significant differences in the weight changes among these groups within 10 days (Figure 6B). However, the tumors in the mice without a light treatment exhibited apparent growth compared with the treatment groups. Remarkably, tumor growth in the mice receiving the DOX-loaded Meso-CNs was effectively inhibited after NIR laser irradiation as a result of the combined chemo-photothermal therapy (Figure 6C). Several tumors in the treatment groups were completely eradicated (Figure 6D). The mice were sacrificed on the 10th day, and we collected their tumors and major organs for histology analyses by hematoxylin and eosin (H&E) staining. The staining results of the tumor sections further confirmed that the cells in the tumors injected with Meso-CNs (or Meso-CNs+DOX) followed by laser irradiation (both 808 nm and 1120 nm) were damaged significantly, whereas the tumor cells in control groups largely retained their normal morphologies with distinctive membrane and nuclear structures. Furthermore, the histological assessment confirmed that there was no damage or inflammation in the major organs of each group (Figure 6E and Figure S7).

Conclusions

In conclusion, we demonstrated that the Meso-CNs prepared by a facile "silica-assisted" method possess intense broad absorption in the UV–NIR wavelength region and exhibit excellent photothermal conversion and photoacoustic generation. The absorption coefficients of Meso-CNs are 1.5–2 times higher than those of SWCNTs and graphene in the UV–Vis–NIR wavelength region and are comparable to those of GNRs in both the NIR-I and NIR-II optical windows of tissue. Importantly, DOX was loaded into the Meso-CNs with a high efficiency owing to the appropriate pore sizes and large surface area of the Meso-CNs, which could be utilized for the enhanced killing of cancer cells by chemotherapeutics. *In vivo* chemo-photothermal combination therapy was demonstrated using DOX-loaded Meso-CNs, achieving a remarkable tumor growth inhibition effect under NIR laser treatment. The integrated nanomedicine platform exhibits great promise as a highly versatile multimodal theranostic agent against cancers.

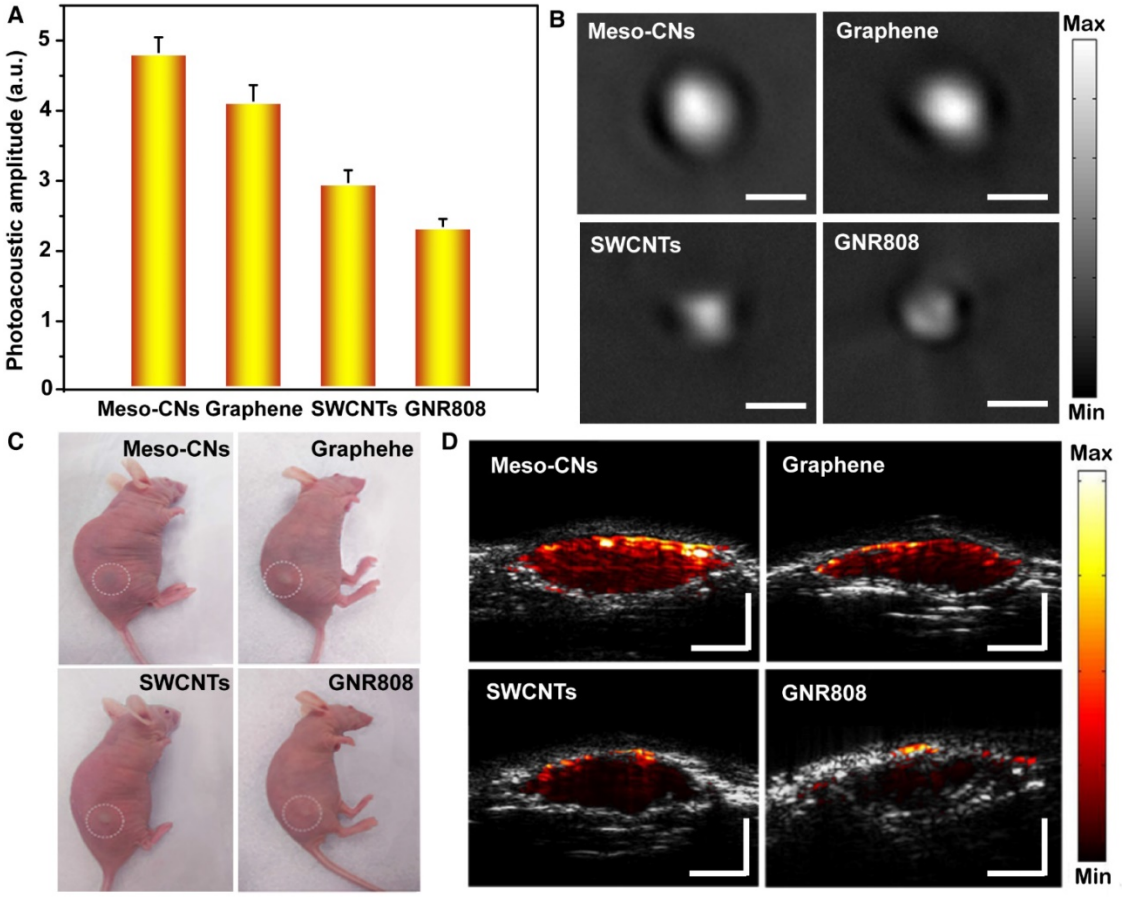

Figure 5. Comparison of the photoacoustic properties of Meso-CNs with graphene, SWCNTs, and GNR808. (A) Photoacoustic amplitudes of the photoacoustic reagents based on the same concentration (25 μg/mL) in an agar phantom. **(B)**. Photoacoustic images of the photoacoustic reagents based on the same concentration (25 μg/mL) in an agar phantom. **(C)** Photographs of nude mice subcutaneously injected with the photoacoustic reagents. **(D)** Photoacoustic/ultrasound co-registered images of the photoacoustic reagents based on the same concentration (25 μg/mL) *in vivo*. Depth and scale bars: 2 mm.

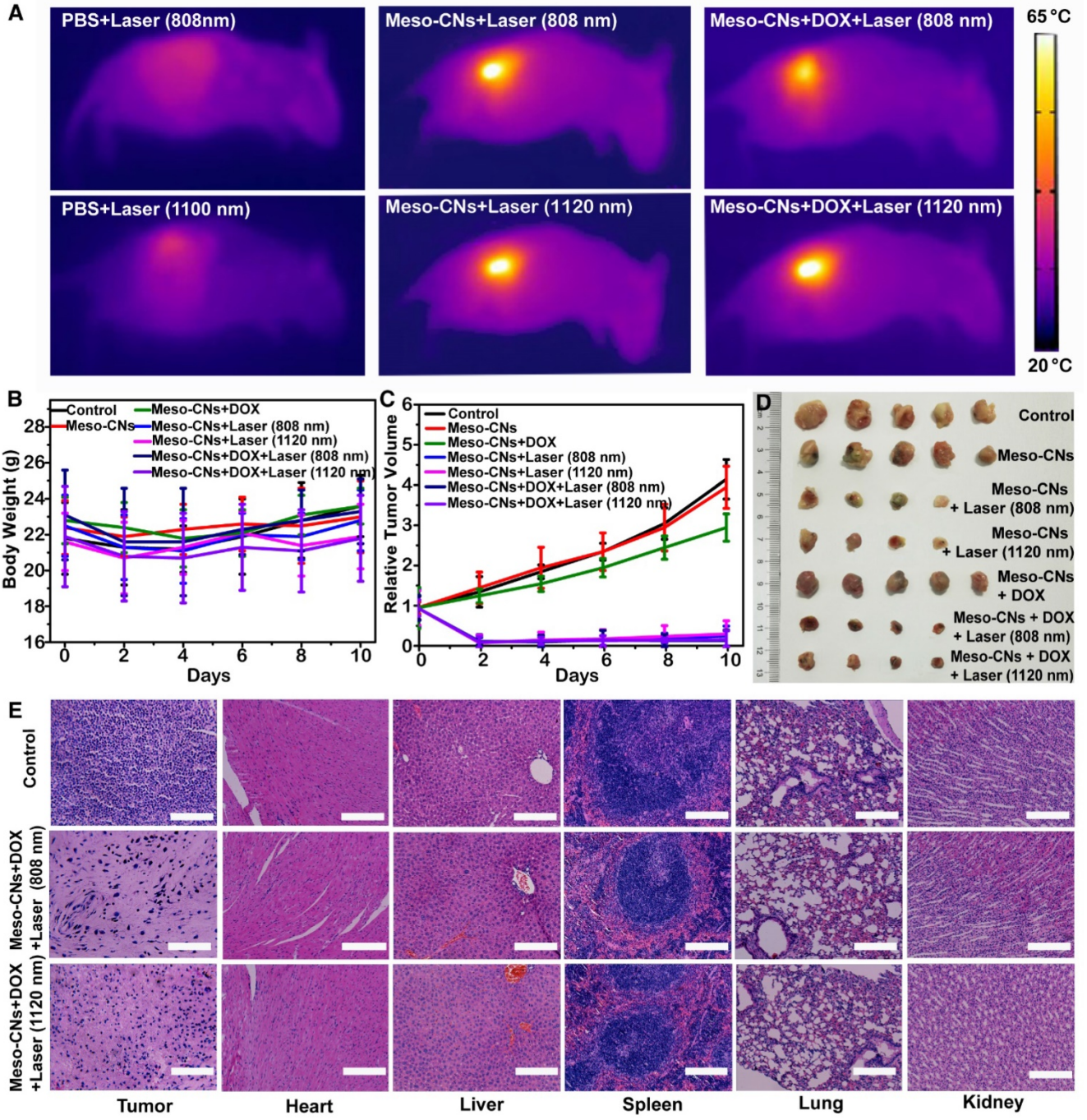

Figure 6. ***In vivo*** **photothermal therapy. (A)** IR thermal images of tumor-bearing mice following intratumoral injection of PBS, Meso-CN, or DOX-loaded Meso-CN solutions under 808 nm or 1120 nm laser irradiation at a power density of 0.5 W/cm^2 for 15 min. **(B)** Average body weight of mice after various treatments. Five mice were used in each group. **(C)**. H22 tumor-growth curves of mice after various treatments. The relative tumor volumes were normalized to their initial sizes. **(D)**. Photograph of the tumors collected from different groups of mice on the 10th day post treatment. Note that in the laser-treatment groups, some tumors were completely eliminated after treatment. **(E)**. H&E-stained tumor and major organ tissue slices collected from mice post various treatments. Scale bar: 200 μm.

Materials and Methods

Synthesis of Meso-CNs

In a typical synthesis of Meso-CNs, 0.1 mL ammonia aqueous solution (NH_4OH, 25 wt%) was mixed with 7 mL absolute ethanol solution, 1.04 g hexadecyl trimethylammonium chloride (CTAC) solution (25 wt% in water), and 20 mL H_2O. The mixture was stirred for 30 min. 0.2 g resorcinol was added to the reaction solution and stirred for further 30 min. Subsequently, 0.36 mL tetraethylorthosilicate (TEOS) and 0.28 mL formaldehyde solution were added and stirred for 24 h at 30 °C. The solid product was obtained by centrifugation and air-dried at 60 °C overnight. Then calcination was carried out under a nitrogen atmosphere in a tubular furnace at 200, 350,

500, 600 °C for 2 h with a heating rate of 1 °C/min and at 800 °C for 5 h with a heating rate of 5 °C/min. 10 % hydrofluoric acid was mixed with the product and stirred for 12 h. The Meso-CNs were washed with water and finally collected by centrifugation.

In a typical synthesis of Micro-CNs, 0.01 mL of NH_4OH (25 wt%) was mixed with 2.82 mL absolute ethanol solution, 7.04 mL of deionized water, 0.23 g of CTAB (25 wt% in water) and 0.035 g resorcinol. The mixture was stirred for 30 min at 35 °C. 0.05 mL of formaldehyde solution was added to the reaction solution and stirred for 6 h at 30 °C. After cooling to room temperature, the mixture was aged at room temperature overnight without stirring. Subsequently, the solid product was obtained by centrifugation and air-dried at 60 °C for 48 h. Then calcination was carried out in a tubular furnace at 150 °C for 1 h with a heating rate of 5 °C/min under a nitrogen atmosphere. The temperature was then raised to 800 °C at 5 °C/min and kept for 2 h.

Characterization of Meso-CNs

The morphology and structure of the Meso-CNs and Micro-CNs were investigated by TEM (FEI Tecnai G2 F20 s-twin D573) at 200 kV. SEM characterizations of Meso-CNs were obtained on a JEOL JSM-6700F field-emission scanning electron microscope. The particle size and zeta potential were measured with a Malvern Nano ZS instrument. The nitrogen absorption experiments were performed at 77 K on a Micromeritics Tristar 2420 system with micropore analysis. XPS were recorded on a ESCALAB250 system using a monochromatic Al KαX-ray source (1486.6 eV). The XRD measurements were performed on a Rigaku 2550 diffractometer with Cu Kα radiation (λ = 1.5418 Å).

Meso-CNs and Micro-CNs were dispersed in water at the same concentration and their UV–Vis–NIR absorption spectra were recorded with a SHIMADZU UV-2500 spectrophotometer. SWCNTs and graphene were dispersed in water at different concentrations using sodium dodecyl sulfate as surfactant. Meso-CNs, GNR808 and GNR1120 were dispersed in water at different concentrations without using surfactant. The UV-Vis-NIR absorption spectra of the samples were measured with a SHIMADZU UV-3600 spectrophotometer.

Photothermal conversion measurements

Meso-CN, graphene, SWCNT, GNR808 and GNR1120 water solutions (30 μg/mL, 5.0 mL) were irradiated with a 808 nm laser at a power density of 1 W/cm² for 10 min and a 1120 nm laser at a power density of 0.5 W/cm² for 10 min, respectively. The power density of 1 W/cm² is usually used for 808 nm NIR laser–induced heat conversion. Pure water was used as a negative control. Stirrers were used to keep solutions heated evenly. Temperatures were recorded every 0.5 s by a digital thermometer with a thermocouple probe. The same operations were done on different concentrations of Meso-CN solutions (5, 10, 20, 30 μg/mL). Meso-CN, graphene, SWCNT, GNR808 and GNR1120 water solution at the same concentration (30 μg/mL, 1.0 mL) were irradiated with a 808 nm laser for 3 min and a 1120 nm laser at a power density of 0.5 W/cm² for 3 min, respectively. Real-time thermal images of those samples were recorded with an E8 thermal IR camera (FLIR).

In vitro cytotoxicity assay

The Hela and MCF7 cell lines were used for *in vitro* cytotoxicity assay. The cells were seeded into 96-well plates at a density of 0.8×10^4 cells/well and incubated for 24 h. Then the cells were incubated with 200 μL fresh DMEM culture medium containing Meso-CNs at various concentrations (0, 50, 100, 150 and 200 μg/mL) for 24 h, followed by addition of MTT (5 mg/mL in PBS solution) and another 3 h co-incubation. The growth medium was removed, and 150 μL DMSO was added into each well to dissolve all formed formazan crystals. The spectrophotometric absorbance of the assay was measured using a microplate reader (BioTek Cytation3, USA) at 490 nm to determine the cell viabilities.

In vitro photothermal therapy

Standard MTT assay and Calcein AM and PI co-staining were carried out to determine PTT efficacy of the Meso-CNs *in vitro*. Hela and MCF7 cells were seeded in 96-well plates (0.8×10^4 cells/well) and incubated for 24 h. After rinsing with PBS (pH: 7.3), the Hela and MCF7 cells were incubated with 200 μL fresh DMEM culture medium containing Meso-CNs at various concentrations (0, 10, 30, 50 and 100 μg/mL) for 4 h and then irradiated by a 650 nm red laser at 0.5 W/cm² power density for 30 min. The laser spot was adjusted to fully cover the whole area of each well. The process of MTT assay was then carried out to determine the viabilities of the cancer cells.

MCF7 cells were seeded in 8 glass culture dishes (6×10^4 cells/well) and incubated for 24 h. Then the 8 glass culture dishes were divided into two groups. After rinsing with PBS (pH: 7.3), each group was added into 1 mL fresh DMEM culture medium containing Meso-CNs at various concentrations (0, 10, 20 and 30 μg/mL). After 4 h incubation, one group was irradiated by a 808 nm laser at 1 W/cm² for 10 min and another group was irradiated by a 1120 nm laser at 0.5 W/cm² power density for 20 min.

Afterwards, the treated cells were costained with Calcein AM and PI for 30 min. The cells were rinsed again with PBS and then imaged by an Olympus confocal microscope.

Drug loading and controllable release

DOX (4 mg) and Meso-CNs (4 mg) were dispersed into H_2O. The final volume of the mixture was 32 mL and the mixture was stirred for 24 h at room temperature. The free DOX was removed by centrifuging at 10282 g for 10 min. Then the supernatant solution was collected and its absorbance was measured with a UV-2500. The weight of unloaded DOX was calculated by absorbance using a standard curve of absorbance at different concentrations of DOX (Figure S3A, B). The loading content (LC, w/w%) of DOX was evaluated from the equation:

$$LC_{DOX} = (\text{DOX loading weight} / \text{weight of Meso-CNs}) \times 100\%.$$

Meso-CNs+DOX were collected after centrifugation and the concentration of Meso-CNs was adjusted to 1 mg/mL. The total weight of DOX loaded in Meso-CNs was calculate by LC_{DOX} (35.0%). DOX release was assessed in PBS buffer (pH: 7.2 or 5.2). Briefly, four glass bottles were prepared, 5 mL PBS (pH: 7.2 or 5.2) was added, and they were loaded with a dialysis bag containing 0.43 mL Meso-CNs+DOX. Samples were maintained at 37 °C on a sample heater before treatment, then two samples dispersed in PBS (pH 5.2) were illuminated by 808 nm or 1120 nm laser with a power density of 0.5 W/cm^2. Meanwhile, samples were exposed, or not, to NIR laser repeatedly in 2 h intervals. At every interval, the PBS was replaced and characterized by measuring the UV–Vis–NIR absorption spectra with a UV-2500 spectrophotometer. The release percentages of DOX were calculated by the absorption spectra of the PBS using a standard curve of absorbance at different concentrations of DOX. The release percentages (RP, W/W %) were evaluated from the equation:

$$RP_{DOX} = (\text{DOX release weight} / \text{DOX initial weight}) \times 100\%.$$

Intracellular drug release

DOX (1 mg) and Meso-CNs (1 mg) were dispersed into H_2O. The final volume of the mixture was 8 mL and the mixture was stirred for 24 h at room temperature. The free DOX was removed by centrifuging at 10282 g for 10 min. Then the precipitate of Meso-CNs+DOX was collected and we adjusted the concentration of Meso-CNs to 200 μg/mL.

MCF7 cells (6×10^4 cells/well) were seeded in 6-well plates and incubated for 24 h. Then the growth medium was replaced with Meso-CNs+DOX mixture (0.5 mL) and 2X DMEM (0.5 mL). After 5 h incubation at 37 °C, the mixture medium was removed and MCF7 were washed with PBS (pH: 7.2) three times. Hoechst 332588 was diluted to 5 μg/mL with DMEM/F-12 and added into 6-well plates (1 mL/well). After 0.5 h incubation, MCF7 were washed with PBS (pH: 7.2) three times and then imaged by an Olympus confocal microscope.

Photoacoustic imaging

The photoacoustic tomography (PAT) system used for our experiment is home-made at the Faculty of Health Sciences of the University of Macau. For the phantom experimental test, a square chicken breast (length: 3 mm; width: 2 mm) was embedded into a 3.5 cm diameter solid cylindrical phantom. The phantom materials utilized were composed of Intralipid as scatterer, Meso-CNs and other contrast agents (Graphene, SWCNTs, GNR808) as absorber. Agar powder (1–2%) was used for solidifying the Intralipid, Meso-CNs and other contrast agent solutions. We then immersed the chicken breast solid phantom into a water tank. The 808 nm optical wavelength were used for measurements.

The *in vivo* tests were performed in compliance with the Guidelines for the Care and Use of Research Animals established by the Animal Care and Use Committee at the University of Macau. 8-week-old female nude mice were employed for the present investigation. For imaging, the mice were anaesthetized and injected with Meso-CNs, graphene, SWCNTs or GNR808 into their backside. After adjusting to a suitable position upon the backside of the mice, we performed cross-sectional PAT of those mice and then the data was further processed to generate the images.

In vivo photothermal therapy

The animal experiments were performed strictly in accordance with the governmental guidelines of the Ministry of Science and Technology of the PR China for the Care and Use of Laboratory Animals and were approved by the Animal Care and Use Committee of Jilin University. ICR mice (5-weeks-old, 20–25 g, female) were obtained from Liaoning Chang Sheng Biotechnology Co., Ltd. (Liaoning, China). Three mice were intraperitoneally injected with hepatoma 22 (H22) to form ascites. Then the ascites (120 μL/mouse) were injected subcutaneously into the backside of ICR mice to prepare tumor-bearing mice. When the tumors achieved a surface diameter of 6–7 mm, mice were randomly distributed into seven

groups named (a) Control, (b) Meso-CNs, (c) Meso-CNs+NIR (808 nm), (d) Meso-CNs+NIR (1120 nm), (e) Meso-CNs+DOX, (f) Meso-CNs+DOX+laser (808 nm) and (g) Meso-CNs+DOX+laser (1120 nm) group.

Mice of all groups were anesthetized and correspondingly intratumorally injected as follows: (a) 80 μL PBS; (b), (c) and (d) 80 μL Meso-CNs (0.5 mg/mL); (e), (f) and (g) 80 μL DOX+Meso-CNs (0.5 mg/mL, LC_{DOX}= 30%). Group (c) and (f) were exposed to 808 nm laser at 0.5 W/cm^2 for 20 min at 3 h post injection. Group (d) Meso-CNs+laser (1120 nm) and (g) Meso-CNs+DOX+laser (1120 nm) were exposed to 1120 nm laser at 0.5 W/cm^2 for 20 min at 3 h post injection. Thermal IR imager was used to measure the temperature of the tumor area during the process of laser irradiation. The tumor size and body weight of each mouse were monitored every two days to portray the growth curve post-treatment. The volumes of tumors were evaluated from the formula: width^2×length/2. The relative tumor volume was calculated by normalizing the measured tumor volume size to their initial values. After 10 days, mice were sacrificed and the tumors were collected for further histology analysis. The histopathological tests were performed according to standard laboratory procedures.

Abbreviations

Meso-CNs: mesoporous carbon nanospheres; NIR: near-infrared; NIR-I: the first near-infrared window; NIR-II: the second near-infrared window; DOX: doxorubicin; PTT: photothermal therapy; PAI: photoacoustic imaging; CNTs: carbon nanotubes; SWCNTs: single-walled carbon nanotubess; GO: graphene oxide; GNRs: gold nanorods; TEM: transmission electron microscopy; SEM: scanning electron microscopy; Micro-CNs: microporous carbon nanospheres; BJH: Barrett−Joyner−Halenda; BET: Brunauer–Emmett–Teller; XRD: X-ray diffraction; SAXS: X-ray scattering; XPS: X-ray photoelectron spectroscopy; GNR808: gold nanorods with an absorption peak at 808 nm; GNR1120: gold nanorods with an absorption peak at 1120 nm; MTT: 3-(4,5-dimethylthiazol-2-yl)-2,5-diphenyltetrazolium bromide; H&E: hematoxylin and eosin; CTAC: hexadecyl trimethylammonium chloride; TEOS: tetraethylorthosilicate; RP: release percentage; PAT: photoacoustic tomography.

Acknowledgments

This study was financially supported by the National Natural Science Foundation of China (NSFC 61335001; NSFC 21671073; NSFC 81771930) and Shenzhen Science and Technology Innovation Commission (Grant No. JCYJ20170307110157501). The study was also supported in part by MYRG2015-00036-FHS and MYRG2016-00110-FHS grants from the University of Macau as well as FDCT 026/2014/A1 and FDCT 025/2015/A1 grants from the Macao government.

Supplementary Material

Supplementary figures and tables on structural and optical characterization of Meso-CNs, photothermal conversion and photostability of Meso-CNs, H&E-stained tissue section of tumors and major organs. http://www.thno.org/v08p0663s1.pdf

Competing Interests

The authors have declared that no competing interest exists.

References

1. Qu D, Zheng M, Du P, Zhou Y, Zhang LG, Li D, et al. Highly luminescent S, N co-doped graphene quantum dots with broad visible absorption bands for visible light photocatalysts. Nanoscale. 2013;5:12272-12277.
2. Joseph KLV, Lim J, Anthonysamy A, Kim HI, Choi W, Kim JK. Squaraine-sensitized composite of a reduced graphene oxide/TiO2 photocatalyst: π–π stacking as a new method of dye anchoring. J Mater Chem A. 2015;3:232-239.
3. Ma RY, Wang L, Zhang BS, Yi XF, Zheng AM, Deng F, et al. Rational design of zirconium-doped titania photocatalysts with synergistic bronsted acidity and photoactivity. ChemSusChem. 2016;9:2759-2764.
4. Kim JY, Lee K, Coates NE, Moses D, Nguyen TQ, Dante M, et al. Efficient tandem polymer solar cells fabricated by all-solution processing. Science. 2007;317:222-225.
5. Miao XC, Tongay S, Petterson MK, Berke K, Rinzler AG, Appleton BR, et al. High efficiency graphene solar cells by chemical doping. Nano Lett. 2012;12:2745-2750.
6. Wang X, Zhi LJ, Mullen K. Transparent, conductive graphene electrodes for dye-sensitized solar cells. Nano Lett. 2008;8:323-327.
7. Cao LY, White JS, Park JS, Schuller JA, Clemens BM, Brongersma ML. Engineering light absorption in semiconductor nanowire devices. Nat Mater. 2009;8:643-647.
8. Cao LY, Fan PY, Vasudev AP, White JS, Yu ZF, Cai WS, et al. Semiconductor nanowire optical antenna solar absorbers. Nano Lett. 2010;10:439-445.
9. Chen Y, Xu PF, Wu MY, Meng QS, Chen HR, Shu Z, et al. Colloidal RBC-shaped, hydrophilic, and hollow mesoporous carbon nanocapsules for highly efficient biomedical engineering. Adv Mater. 2014;26:4294-4301.
10. Sun Z, Xie H, Tang S, Yu XF, Guo Z, Shao J, et al. Ultrasmall black phosphorus quantum dots: synthesis and use as photothermal agents. Angew Chem Int Ed. 2015; 127:11688-11692.
11. Cheng XJ, Sun R, Yin L, Chai ZF, Shi HB, Gao MY. Light-triggered assembly of gold nanoparticles for photothermal therapy and photoacoustic imaging of tumors in vivo. Adv Mater.2017;29: 1604894
12. Xiao QF, Zheng XP, Bu WB, Ge WQ, Zhang SJ, Chen F, et al. A core/satellite multifunctional nanotheranostic for in vivo imaging and tumor eradication by radiation/photothermal synergistic therapy. J Am Chem Soc. 2013;135:13041-13048.
13. Chu KF, Dupuy DE. Thermal ablation of tumours: biological mechanisms and advances in therapy. Nat Rev Cancer.2014;14:199-208.
14. Cheng L, Wang C, Feng L, Yang K, Liu Z. Functional nanomaterials for phototherapies of cancer. Chem Rev. 2014;114:10869-10939.
15. Cai Y, Liang PP, Tang QY, Yang XY, Si WL, Huang W, et al. Diketopyrrolopyrrole-triphenylamine organic nanoparticles as multifunctional reagents for photoacoustic imaging-guided photodynamic/photothermal synergistic tumor therapy. ACS Nano. 2017;11:1054-1063.
16. Ng KK, Weersink RA, Lim L, Wilson BC, Zheng G. Controlling spatial heat and light distribution by using photothermal enhancing auto-regulated liposomes (PEARLs). Angew Chem Int Ed. 2016;55:10003-10007.
17. Lu AH, Zhang XQ, Sun Q, Zhang Y, Song QW, Schuth F, et al. Precise synthesis of discrete and dispersible carbon-protected magnetic nanoparticles for efficient magnetic resonance imaging and photothermal therapy. Nano Res. 2016;9:1460-1469.
18. Moon H, Kumar D, Kim H, Sim C, Chang JH, Kim JM, et al. Amplified photoacoustic performance and enhanced photothermal stability of reduced

graphene oxide coated gold nanorods for sensitive photoacoustic imaging. ACS Nano. 2015;9:2711-2719.
19. Liu Y, Yuan Z. Multi-spectral photoacoustic elasticity tomography. Biomed Opt Express. 2016;7:3323-3334.
20. Wang LV. Multiscale photoacoustic microscopy and computed tomography. Nat Photonics. 2009;3:503-509.
21. Ge J, Jia Q, Liu W, Guo L, Liu Q, Lan M, et al. Red-emissive carbon dots for fluorescent, photoacoustic, and thermal theranostics in living mice. Adv Mater. 2015;27:4169-4177.
22. Liu YB, Jiang HB, Yuan Z. Two schemes for quantitative photoacoustic tomography based on Monte Carlo simulation. Med Phys.2016;43:3987-3997.
23. Xie C, Zhen X, Lei QL, Ni R, Pu KY. Self-assembly of semiconducting polymer amphiphiles for in vivo photoacoustic imaging. Adv Funct Mater. 2017;27: 1605397.
24. Lyu Y, Fang Y, Miao QQ, Zhen X, Ding D, Fu KY. Intraparticle molecular orbital engineering of semiconducting polymer nanoparticles as amplified theranostics for in vivo photoacoustic imaging and photothermal therapy. ACS Nano. 2016;10:4472-4481.
25. Liang XL, Li YY, Li XD, Jing LJ, Deng ZJ, Yue XL, et al. PEGylated polypyrrole nanoparticles conjugating gadolinium chelates for dual-modal MRI/photoacoustic imaging guided photothermal therapy of cancer. Adv Funct Mater.2015;25:1451-1462.
26. Ku G, Zhou M, Song SL, Huang Q, Hazle J, Li C. Copper sulfide nanoparticles as a new class of photoacoustic contrast agent for deep tissue imaging at 1064 nm. ACS Nano. 2012;6:7489-7496.
27. Kim JW, Galanzha EI, Shashkov EV, Moon HM, Zharov VP. Golden carbon nanotubes as multimodal photoacoustic and photothermal high-contrast molecular agents. Nat Nanotechnol. 2009;4:688-694.
28. Eghtedari M, Oraevsky A, Copland JA, Kotov NA, Conjusteau A, Motamedi M. High sensitivity of in vivo detection of gold nanorods using a laser optoacoustic imaging system. Nano Lett. 2007;7:1914-1918.
29. Tsai MF, Chang SHG, Cheng FY, Shanmugam V, Cheng YS, Su CH, et al. Au nanorod design as light-absorber in the first and second biological near-infrared windows for in vivo photothermal therapy. ACS Nano. 2013;7:5330-5342.
30. Yang JP, Shen DK, Zhou L, Li W, Li XM, Yao C, et al. Spatially confined fabrication of core-shell gold nanocages@mesoporous silica for near-infrared controlled photothermal drug release. Chem Mater. 2013;25:3030-3037.
31. Huang P, Qian XQ, Chen Y, Yu LD, Lin H, Wane LY, et al. Metalloporphyrin-encapsulated biodegradable nanosystems for highly efficient magnetic resonance imaging-guided sonodynamic cancer therapy. J Am Chem Soc. 2017; 139:1275-1284.
32. Li K, Liu B. Polymer-encapsulated organic nanoparticles for fluorescence and photoacoustic imaging. Chem Soc Rev. 2014;43:6570-6597.
33. Xie C, Upputuri PK, Zhen X, Pramanik M, Pu K. Self-quenched semiconducting polymer nanoparticles for amplified in vivo photoacoustic imaging. Biomaterials. 2016;119:1-8.
34. Zhang J, Chen HB, Zhou T, Wang LM, Gao DY, Zhang XJ, et al. A PIID-DTBT based semi-conducting polymer dots with broad and strong optical absorption in the visible-light region: highly effective contrast qgents for multiscale and multi-spectral photoacoustic imaging. Nano Res. 2017;10:64-76.
35. Pu K, Mei JG, Jokerst JV, Hong GS, Antaris AL, Chattopadhyay N, et al. Diketopyrrolopyrrole-based semiconducting polymer nanoparticles for in vivo photoacoustic imaging. Adv Mater. 2015;27:5184-5190.
36. Lyu Y, Zhen X, Miao YS, Pu KY. Reaction-based semiconducting polymer nanoprobes for photoacoustic imaging of protein sulfenic acids. ACS Nano. 2017;11:358-367.
37. Georgakilas V, Tiwari JN, Kemp KC, Perman JA, Bourlinos AB, Kim KS, et al. Noncovalent functionalization of graphene and graphene oxide for energy materials, biosensing, catalytic, and biomedical applications. Chem Rev.2016;116:5464-5519.
38. Li D, Han D, Qu SN, Liu L, Jing PT, Zhou D, et al. Supra-(carbon nanodots) with a strong visible to near-infrared absorption band and efficient photothermal conversion. Light-Sci Appl. 2016;5:e16120.
39. Yang J, Ma MZ, Li LQ, Zhang YF, Huang W, Dong XC. Graphene nanomesh: new versatile materials. Nanoscale. 2014;6:13301-13313.
40. Kam NWS, O'Connell M, Wisdom JA, Dai HJ. Carbon nanotubes as multifunctional biological transporters and near-infrared agents for selective cancer cell destruction. Proc Natl Acad Sci USA. 2005;102:11600-11605.
41. Zhou MY, Liu SH, Jiang YQ, Ma HR, Shi M, Wang QS, et al. Doxorubicin-loaded single wall nanotube thermo-sensitive hydrogel for gastric cancer chemo-photothermal therapy. Adv Funct Mater. 2015;25:4730-4739.
42. Chakravarty P, Marches R, Zimmerman NS, Swafford ADE, Bajaj P, Musselman IH, et al. Thermal ablation of tumor cells with antibody-functionalized single-walled carbon nanotubes. Proc Natl Acad Sci USA. 2008;105:8697-8702.
43. Wang CH, Huang YJ, Chang CW, Hsu WM, Peng CA. In vitro photothermal destruction of neuroblastoma cells using carbon nanotubes conjugated with GD2 monoclonal antibody. Nanotechnology 2009;20: 315101.
44. Robinson JT, Welsher K, Tabakman SM, Sherlock SP, Wang HL, Luong R, et al. High performance in vivo near-IR (> 1 μm) imaging and photothermal cancer therapy with carbon nanotubes. Nano Res. 2010;3:779-793.
45. Kostarelos K, Bianco A, Prato M. Promises, facts and challenges for carbon nanotubes in imaging and therapeutics. Nat Nanotechnol. 2009;4:627-633.
46. Liu CH, Wang Z, Jia HX, Li ZP. Efficient fluorescence resonance energy transfer between upconversion nanophosphors and graphene oxide: a highly sensitive biosensing platform. Chem Commun. 2011;47:4661-4663.
47. Zhou M, Zhai YM, Dong SJ. Electrochemical sensing and biosensing platform based on chemically reduced graphene oxide. Anal Chem. 2009;81:5603-5613.
48. Hong H, Zhang Y, Engle JW, Nayak TR, Theuer CP, Nickles RJ, et al. In vivo targeting and positron emission tomography imaging of tumor vasculature with ^{66}Ga labeled nano-graphene. Biomaterials. 2012;33:4147-4156.
49. Shi SX, Yang K, Hong H, Valdovinos HF, Nayak TR, Zhang Y, et al. Tumor vasculature targeting and imaging in living mice with reduced graphene oxide. Biomaterials. 2013;34:3002-3009.
50. Wang Y, Wang KY, Zhao JF, Liu XG, Bu J, Yan XY, et al. Multifunctional mesoporous silica-coated graphene nanosheet used for chemo-photothermal synergistic targeted therapy of glioma. J Am Chem Soc. 2013;135:4799-4804.
51. Feng LZ, Yang XZ, Shi XZ, Tan XF, Peng R, Wang J, et al. Polyethylene glycol and polyethylenimine dual-functionalized nano-graphene oxide for photothermally enhanced gene delivery. Small. 2013;9:1989-1997.
52. Yao XX, Tian ZF, Liu JX, Zhu YF, Hanagata N. Mesoporous silica nanoparticles capped with graphene quantum dots for potential chemo-photothermal synergistic cancer therapy. Langmuir 2017; 33: 591-599.
53. Yao XX, Niu XX, Ma KX, Huang P, Grothe J, Kaskel S, et al. Graphene quantum dots-capped magnetic mesoporous silica nanoparticles as a multifunctional platform for controlled drug delivery, magnetic hyperthermia, and photothermal therapy. Small 2017; 13: 1602225.
54. Yang K, Hu LL, Ma XX, Ye SQ, Cheng L, Shi XZ, et al. Multimodal imaging guided photothermal therapy using functionalized graphene nanosheets anchored with magnetic nanoparticles. Adv Mater. 2012;24:1868-1872.
55. Robinson JT, Tabakman SM, Liang YY, Wang HL, Casalongue HS, Vinh D, et al. Ultrasmall reduced graphene oxide with high near-infrared absorbance for photothermal therapy. J Am Chem Soc. 2011;133:6825-6831.
56. Chen YW, Su YL, Hu SH, Chen SY. Functionalized graphene nanocomposites for enhancing photothermal therapy in tumor treatment. Adv Drug Deliver Rev. 2016;105:190-204.
57. Rong PF, Yang K, Srivastan A, Kiesewetter DO, Yue XY, Wang F, et al. Photosensitizer loaded nano-graphene for multimodality imaging guided tumor photodynamic therapy. Theranostics. 2014;4:229-239.
58. Tian B, Wang C, Zhang S, Feng LZ, Liu Z. Photothermally enhanced photodynamic therapy delivered by nano-graphene oxide. ACS Nano. 2011;5:7000-7009.
59. Qiao ZA, Guo BK, Binder AJ, Chen JH, Veith GM, Dai S. Controlled synthesis of mesoporous carbon nanostructures via a "silica-assisted" strategy. Nano Lett. 2013;13:207-212.
60. Wang H, Di J, Sun YB, Fu JP, Wei ZY, Matsui H, et al. Biocompatible PEG-chitosan@carbon dots hybrid nanogels for two-photon fluorescence imaging, near-infrared light/pH dual-responsive drug carrier, and synergistic therapy. Adv Funct Mater. 2015;25:5537-5547.
61. Wang H, Sun YB, Yi JH, Fu JP, Di J, Alonso AD, et al. Fluorescent porous carbon nanocapsules for two-photon imaging, NIR/pH dual-responsive drug carrier, and photothermal therapy. Biomaterials. 2015;53:117-126.
62. Xu GJ, Liu SJ, Niu H, Lv WP, Wu RA. Functionalized mesoporous carbon nanoparticles for targeted chemo-photothermal therapy of cancer cells under near-infrared irradiation. RSC Adv. 2014;4:33986-33997.
63. Zhou L, Dong K, Chen ZW, Ren JS, Qu XG. Near-infrared absorbing mesoporous carbon nanoparticle as an intelligent drug carrier for dual-triggered synergistic cancer therapy. Carbon. 2015;82:479-488.
64. Zhao WR, Wang Y, Yang Y, Tang J, Yang YA. Carbon spheres supported visible-light-driven CuO-BiVO4 heterojunction: preparation, characterization, and photocatalytic properties. Appl Catal B-Environ. 2012;115:90-99.
65. Wang SH, Shang L, Li LL, Yu YJ, Chi CW, Wang K, et al. Metal-organic-framework-derived mesoporous carbon nanospheres containing porphyrin-like metal centers for conformal phototherapy. Adv Mater. 2016;28:8379-8387.
66. Chen H, Zhang J, Chang K, Men X, Fang X, Zhou L, et al. Highly absorbing multispectral near-infrared polymer nanoparticles from one conjugated backbone for photoacoustic imaging and photothermal therapy. Biomaterials 2017;144:42-52.
67. Li L, Chen C, Liu H, Fu C, Tan L, Wang S, et al. Multifunctional carbon-silica nanocapsules with gold core for synergistic photothermal and chemo-cancer therapy under the guidance of bimodal imaging. Adv Funct Mater. 2016;26:4252-4261.